JOURNAL OF PROPULSION AND POWER
Vol. 11, No. 1, January–February 1995

Investigation of Three-Dimensional Flowfield at the Exit of a Turbine Nozzle

M. Zaccaria* and B. Lakshminarayana†
Pennsylvania State University, University Park, Pennsylvania 16802

The objective of the research reported in this article is to gain a detailed understanding of the flowfield at the exit of turbine nozzles. The flowfield was measured at two axial locations downstream of the nozzle of a single-stage turbine with a miniature five-hole probe. An area traverse was carried out to resolve the flowfield accurately, including the nozzle wake, secondary flow region, horseshoe vortex, and losses. All three components of the velocity, stagnation pressure, static pressure, and pitch and yaw angles have been resolved accurately. A distinct vortex core has been observed near the tip and at the hub. The indications are that the horseshoe vortex and the passage vortex have merged to produce a single-loss core region. Roughly, a third of the blade height passage near the tip and a third of the blade height near the hub is dominated by secondary flow phenomena. Only the middle third of the nozzle behaves according to design. The nozzle wake decay is compared to the wake decay of other blades. The nozzle wake decays much faster than a compressor cascade wake, an annular turbine nozzle cascade wake, or a turbine nozzle wake with a large rotor-stator spacing. This faster decay is attributed to effect of the downstream rotor at very small rotor-stator spacing (20% of nozzle axial chord). These and other data are presented, interpreted, and synthesized to understand the nozzle flowfield.

Nomenclature

C = axial chord length at midspan
H = spanwise distance, $(R - R_h)/(R_t - R_h)$
L = semiwake width, wake width at half the depth $V_c/2$
P = total pressure
p = static pressure
R = radius
Re = Reynolds number
r, θ, x = radial, tangential, and axial coordinates, respectively
S = blade spacing
S = percentage pitchwise distance from the wake center at midspan, positive on pressure side, negative on suction side
U_m = blade speed at mean radius
V = total velocity normalized by U_m
V_c = defect in velocity at the wake centerline normalized by U_m
V_{sec} = secondary velocity, Eq. (1)
X = axial distance from nozzle leading edge
Z = axial distance from nozzle trailing edge normalized by axial chord
α = radial flow angle, measured from the cylindrical plane
β = yaw angle measured from axial direction
β_o = vane outlet angle
β_p = primary flow angle
ψ_{LOSS} = total pressure loss coefficient, $(P_{o1} - P_{o2})/0.5\rho U_m^2$
ψ_d = static pressure difference in the wake, $(p_{max} - p_{min})/(p_{max} - p_{min})_{TE}$
ψ_p = nozzle static pressure drop coefficient, $(p_1 - p_2)/0.5\rho U_m^2$
ω = vorticity, Eq. (2)
ω_s = streamwise vorticity normalized by V_{x1}/C

Subscripts

h, t = hub and tip
max = maximum value
min = minimum value
o = stagnation
r, Θ, x = radial, tangential, and axial components
s, n, r = streamwise, principal normal, and radial components
TE = trailing edge
1, 2 = inlet and exit

Superscripts

$-$ = circumferentially mass-averaged
$=$ = area-averaged

Introduction

THE flowfield in an axial flow turbine nozzle is complex, including the presence of three-dimensional boundary layers on the blades and wakes, horseshoe and passage vortices, annulus, and the hub wall boundary layers and secondary flows in the annulus and hub wall boundary layers. Nozzle wakes are a major source of losses, inefficiency, vibration, and noise. The three-dimensional characteristics of the wake, the decay characteristics, and the path that the wake follows is important in the design of the following blade rows. This information is essential for the prediction of the aerodynamic and mechanical performance of a turbine. An understanding of the wake development and its decay is also essential because of the role it plays in the rotor-stator interaction.[1]

Although there has been extensive research done on compressor wakes,[2,3] not much work has been done on turbine wakes. Mee et al.[4] measured the wake of a transonic turbine cascade, Sitaram and Govardhan[5] reported wake data of a very high turning turbine rotor cascade blade, Goldman and Seasholtz[6] measured the wake in an annular turbine cascade, and Dring et al.[7] reported wake data at one axial location in a $1\frac{1}{2}$-stage axial flow turbine with a rotor-nozzle spacing of

Presented as Paper 92-3326 at the AIAA/SAE/ASME/ASEE 28th Joint Propulsion Conference and Exhibit, Nashville, TN, July 6–8, 1992; received Aug. 17, 1992; revision received March 21, 1994; accepted for publication April 19, 1994. Copyright © 1994 by M. Zaccaria and B. Lakshminarayana. Published by the American Institute of Aeronautics and Astronautics, Inc., with permission.

*Graduate Student; currently at the Knolls Atomic Power Laboratory.

†Evan Pugh Professor of Aerospace Engineering, Department of Aerospace Engineering, 153 Hammond Building.

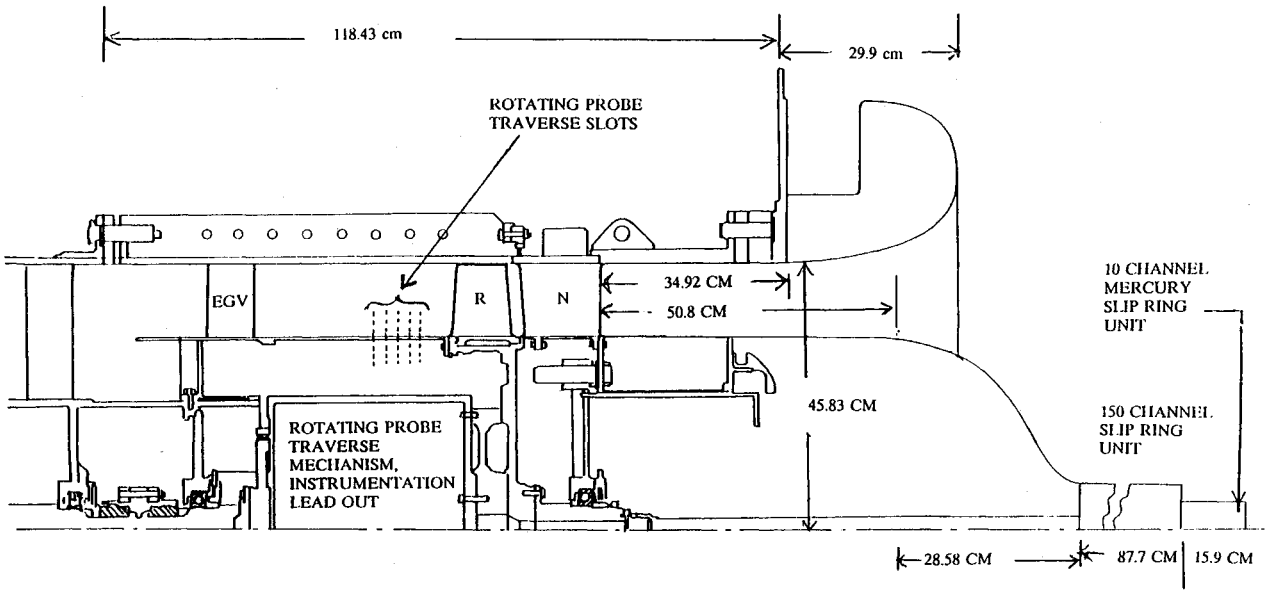

Fig. 1 Schematic and flow path of the AFTRF.

50% nozzle axial chord. Only one of these[7] had a realistic three-dimensional configuration with a rotor downstream. Dring et al.'s rotor was located at 50% nozzle axial chord, which is much higher than usually employed in industry. Furthermore, the wake was measured at only one axial location. Thus, there is a need for a comprehensive survey of the wake at different axial and spanwise locations for a turbine nozzle with a realistic axial distance between the nozzle and the rotor.

A comprehensive description and review of the secondary flowfield in a linear turbine cascade has been given by Langston,[8] Sieverding,[9] and Sharma and Butler[10] among others, and will not be repeated here for brevity.

The objective of this research is to gain a better understanding of the flow inside and downstream of an axial flow turbine nozzle, including three-dimensional viscous and inviscid effects, and annulus and hub wall boundary-layer development, including the horseshoe and passage vortices. The nozzle wake is studied in detail in order to determine the rate of the wake decay in the presence of a rotor in close proximity downstream. These will be useful for a better understanding of rotor-stator interaction, due to viscous wake/secondary flow interaction with the rotor. The comprehensive data acquired with the miniature probe also provides validation data for three-dimensional Navier-Stokes codes.

The data reported in this article is part of a major initiative to understand and comprehend the unsteady flowfield caused by rotor-stator interaction. The data upstream of the rotor (reported in this article) will be correlated with the rotor unsteady flowfield data to be undertaken shortly.

Experimental Facility, Instrumentation and Technique

The Axial Flow Turbine Research Facility (AFTRF) of the Pennsylvania State University is an open-circuit facility 91.66 cm (3 ft) in diam, with a hub-to-tip radius ratio of 0.73, with an advanced axial turbine blading configuration designed by GE Aircraft Engine personnel. The facility consists of a large bellmouth inlet, a turbulence generating grid section, followed by a test section with a nozzle vane guide row and a rotor as shown in Fig. 1. There are 23 nozzle guide vanes and 29 rotor blades followed by outlet guide vanes. Detailed design of the facility, performance, and geometric features are described in Lakshminarayana et al.[11] Figure 2 shows the nozzle vane profile. Some important performance and geometrical parameters are given in Table 1. All of the present experiments were carried out at 20% nozzle-rotor spacing.

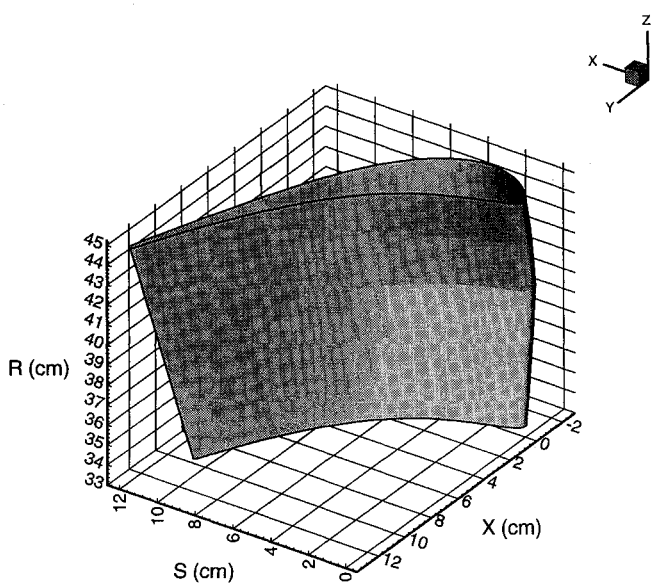

Fig. 2 Nozzle vane profile.

Table 1 Design feature of the AFTRF

Hub/tip ratio	0.7269
Tip radius	0.4582 m
Nozzle guide vane	
Number	23
Chord, tip	0.1768 m
Spacing, tip	0.1308 m
Turning angle	70 deg
Nozzle/rotor gap, tip	0.20–0.50C
Nozzle Reynolds number, based on V_2	10^6
Rotor speed	1300 rpm
Mass flow rate	11.05 kg/s

The nozzle exit flow measurements were carried out using a miniature five-hole probe, with a probe head diameter of 1.67 mm. The exit flow is measured at 50–80 tangential locations in one passage, and at 21 radial locations at X/C = 1.025 and 1.09, and at midspan at X/C = 1.007, 1.01, 1.12, and 1.16. The estimated errors in the five-hole probe measurements are given by Zaccaria and Lakshminarayana,[12] and will not be repeated here for brevity.

Flowfield at Nozzle Exit

The data on nozzle exit flow is presented in this section. For the following plots, the tangential distance is normalized by the nozzle pitch, where $S = 0$ is the wake center at midspan at $X/C = 1.025$. The positive values of S are on the pressure side of the wake, and the negative values of S are on the suction side. The pitchwise extent of the plots is a little less than one blade pitch for both $X/C = 1.025$ and $X/C = 1.09$.

Total Pressure Loss and Static Pressure Drop

The contours of ψ_{LOSS} are shown for $X/C = 1.025$ in Fig. 3. There are two high-loss regions, one near $H = 0.10$ and the other near $H = 0.80$ for both axial locations. These two high-loss regions are caused by secondary flow vortices and their dissipation. The maximum loss regions occur close to the suction surface. Furthermore, the tip loss core is located further from the casing than the loss core near the hub wall. This is caused by the radial inward velocities that exist in the wake and in the freestream region. The circumferentially mass-averaged total pressure loss coefficient is given in Fig. 4. The two loss peaks can be seen clearly in this figure. The peak near the hub is larger in magnitude, but smaller in radial extent than the one near the casing. The larger inlet casing boundary-layer thickness results in larger extent of the secondary flow in this region. The larger magnitude of the hub loss region is a result of the radial inward flow inside the wake, which causes the low momentum fluid in the wake to move toward the hub. Both Yamamoto and Yanagi[13] and Hunter[14] report similar distributions in their annular nozzle cascades.

At midspan, the secondary flow effects are absent, and the mass-averaged loss coefficient is the profile loss coefficient for the vane, which is 0.05. This is close to the value of 0.06 predicted from the correlation by Kacker and Okapuu,[15] which is shown in Fig. 4. The area averaged $\bar{\psi}_{LOSS}$ is calculated to be 0.077 at $X/C = 1.025$ and 0.0818 at $X/C = 1.09$. The losses increase as flow travels downstream of the rotor due to mixing of the wake, the decay of the vortices, and the growth of the endwall boundary layer. The secondary flow loss is the loss calculated by subtract-ing the profile loss from the total loss. The mass-averaged secondary flow loss coefficient measured in this nozzle is equal to 0.0262. This is less than the value of secondary flow loss coefficient predicted from the correlation by Dunham[16] (0.0503). There are two main reasons for this difference. The first is that Dunham's formula overestimates the secondary loss parameter for low-aspect ratio blades. Kacker and Okapuu[15] have derived a correlation for low-aspect ratio blades to include the dependence on aspect ratio. Substituting Kacker and Okapuu's aspect ratio dependence formula into Dunham's secondary loss prediction yields a value of 0.0361 for the secondary loss coefficient, which is much closer, but still higher than the measured value. The second reason for this difference is that the secondary flow loss correlations were developed from cascade loss data taken between 0.7–1.0 chord downstream of the blade, and thus include the additional losses due to mixing, decay of the secondary vortices, and boundary-layer growth. Moore and Adhye[17] measured the losses at three axial planes (from $X/C = 1.1$ to $X/C = 1.4$) downstream of a turbine cascade. Extrapolating their data, the nozzle secondary flow losses are found to increase by 30% from trailing edge to 0.70 chord downstream. Applying this correction to Dunham's correlation results in a value of 0.0253 that is within 2% of the measured secondary flow loss coefficient, 0.0262.

Contours of static pressure drop coefficient and the mass average distribution of static pressure drop coefficient are given in Figs. 5 and 4, respectively. The mass-averaged experimental values are compared to the design values that were calculated using a two-dimensional throughflow analysis that solved the circumferentially averaged equations of motion in the meridional plane using a streamline curvature technique.[11] The presence of strong radial pressure gradient is evident in these figures. The static pressures are generally lower in secondary vortex regions and higher in the wake regions. (Higher static pressure coefficient indicates lower static pressure.) Detailed interpretation of the static pressure across the wake is discussed later in the article.

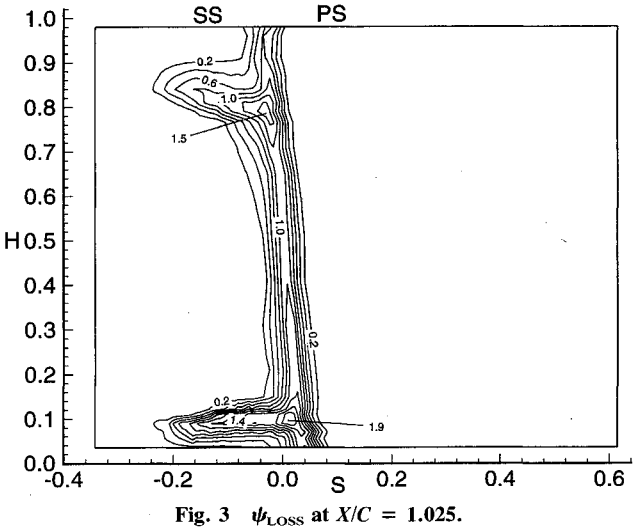

Fig. 3 ψ_{LOSS} at $X/C = 1.025$.

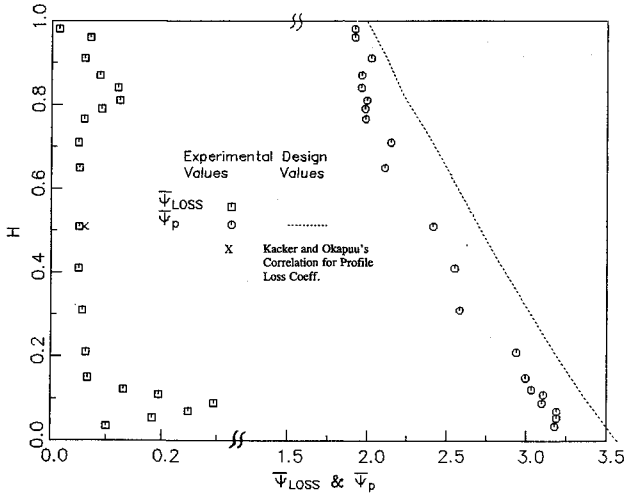

Fig. 4 Circumferentially mass-averaged pressures at $X/C = 1.025$.

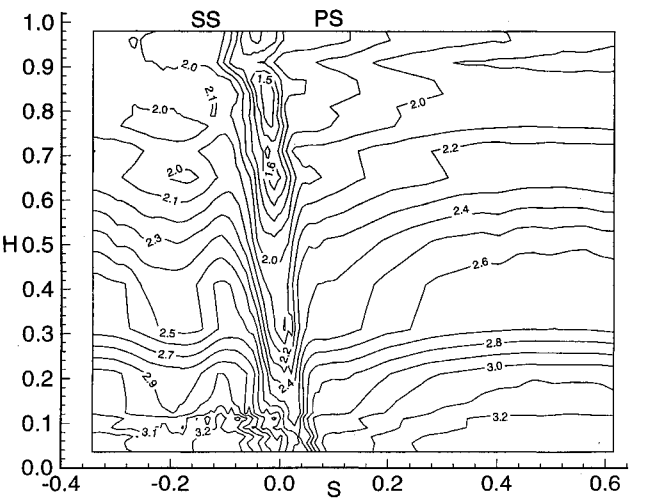

Fig. 5 ψ_p at $X/C = 1.025$.

Velocity and Flow Angles

The circumferentially mass-averaged velocities are shown plotted in Fig. 6. The total and tangential velocity plots show a decrease in velocity near $H = 0.1$ and 0.8, which is due to the hub and tip wall secondary flows. The axial velocity profiles show a decrease near the endwalls, due to the presence of the wall boundary layers. The total, axial, and tangential velocities are in agreement with the design values near midspan region, while deviating from the design values in the secondary flow regions near the endwalls.

A contour plot of the yaw angles β at $X/C = 1.025$ is shown in Fig. 7. The flow is underturned on the pressure side of the wake, and overturned on the suction side of the wake away from the endwalls. This is because the suction surface blade angle is higher than the design exit flow angle (70 deg), and the pressure side blade angle is lower than the design exit flow angle at the trailing edge. This over- and underturning of the flow decreases as the flow travels downstream of the trailing edge from a value of 6 deg of both over- and underturning at $X/C = 1.025$ (midspan) to 2 deg of both over- and underturning at $X/C = 1.09$ (midspan, not shown), which is a result of mixing of the wake. At $X/C = 1.025$, the maximum underturning occurs near $H = 0.1$ and $H = 0.8$. This local underturning of the flow is caused by secondary flow vortices. In the core region of these vortices, underturning as high as 25 deg is observed at $H = 0.80$, whereas near the hub the maximum underturning is 15 deg. There is an overturning of 11 deg near the suction side of the wake at $H = 0.80$ and of 8 deg near the hub wall. This phenomena is as expected from secondary flow theories, and this overturning and underturning of the flow located next to each other is another indication of the presence of vortices at these locations. The mass-averaged yaw angle, presented in Fig. 8, shows the overturning near the casing and near the hub endwall due to secondary flow and vortices. The closest measurement at the casing endwall is 4.5% of the span from the casing, whereas the closest measurement to the hub is 3.0% from the hub. As one moves away from the endwalls the flow becomes underturned, achieving design flow near 20% of span from the hub and 30% of span from the casing. The larger underturned region near the casing is due to the larger secondary flow region near the casing. This is consistent with predictions from secondary flow theories and measurement by others. The experimental values of yaw angle match the design values well near the midspan, while deviating from design in the secondary flow regions, which is expected, since the design code is two dimensional.

The contours of radial flow angles $\propto$ are shown in Fig. 9. The flow is directed toward the hub over most of the passage in the inviscid region. This is due to the radially inward lean of the nozzle trailing edge (see Fig. 2). Binder and Romey,[18] who have a radially inward lean of their nozzle trailing edge, also see radially inward flow over most of the span just downstream of the trailing edge of their annular nozzle cascade. Very high negative radial flow angles or pitch angles (-66 deg) occur at $H = 0.83$ near the suction side of the wake,

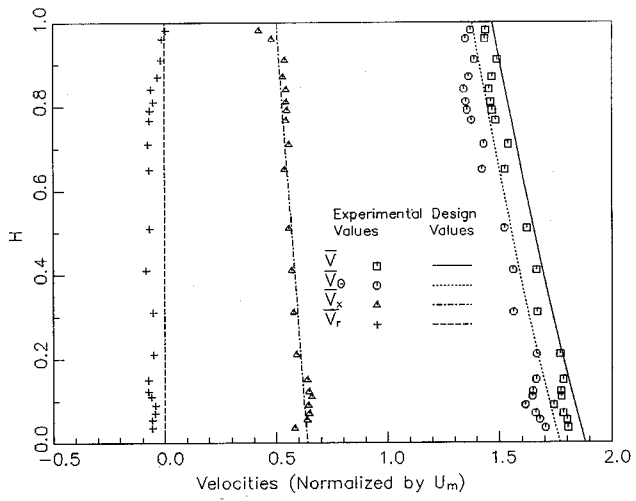

Fig. 6 Circumferentially mass-averaged velocities at $X/C = 1.025$.

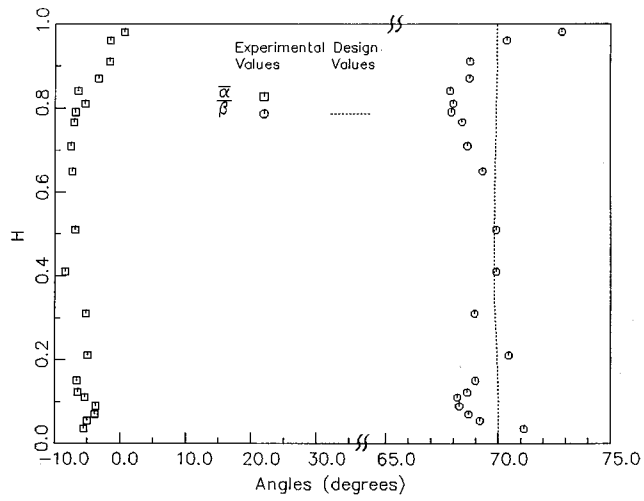

Fig. 8 Circumferentially mass-averaged angles at $X/C = 1.025$.

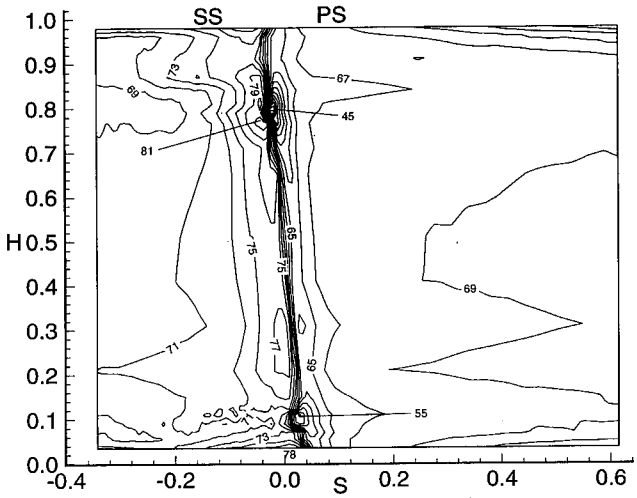

Fig. 7 Yaw angle β at $X/C = 1.025$.

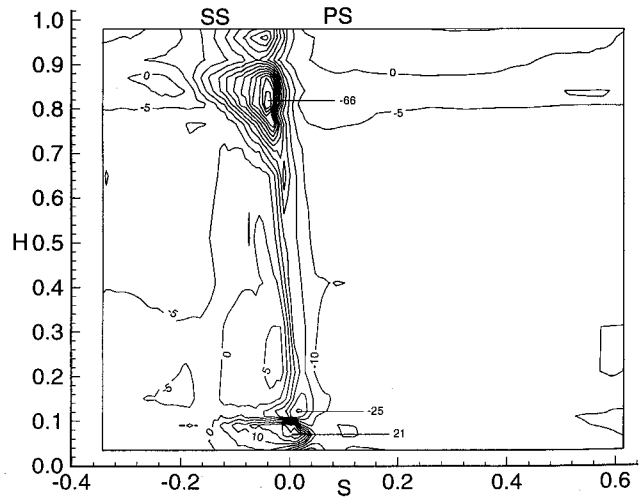

Fig. 9 α at $X/C = 1.025$ (negative values indicate radially inward flow).

whereas positive angles occur at $S = -0.25$, at the same radial location. Also, high negative radial flow angles (−25 deg) occur at $H = 0.13$ and $S = 0$ deg, whereas positive angles (21 deg) occur closer to the hub. This is another indication of the presence of vortices, since local high and low radial flow angles occur across a vortex. The mass-averaged radial flow angles are shown in Fig. 8. The radial flow angles are negative over most of the span, reaching zero at the casing. The negative radial flow angles at the hub are due to the slot that separates the rotating hub from the stationary hub, which is located just downstream of this location.

Secondary Flow Velocity

The secondary flow velocity vectors are shown in Figs. 10 and 11, for $X/C = 1.025$ and 1.09, respectively. The secondary flow vectors in the r-θ plane are derived from the measured data and the design flow angle (70 deg), using the measured radial flow and yaw angles. Using this procedure, the secondary velocities (vectorial) were derived from

$$V_{\text{sec}} = rV_r + nV_n = (V)_{\text{measured}} - (V)_{\text{design}} \qquad (1)$$

where V_r is the radial velocity, and V_n is the velocity normal to the streamwise direction (estimated as indicated above). The presence of strong radial inward flow in the wake can be seen. Strong radial inward flow at the wake center near the casing is caused by the passage vortex (clockwise), which augments the radial inward flow of the wake. The passage

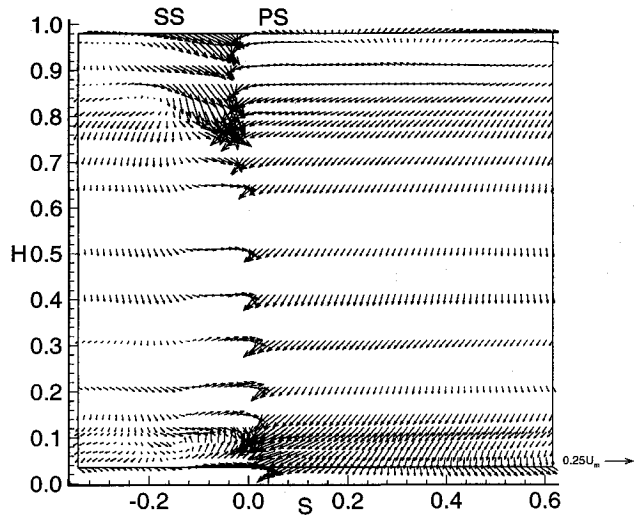

Fig. 10 Secondary velocity vectors at $X/C = 1.025$.

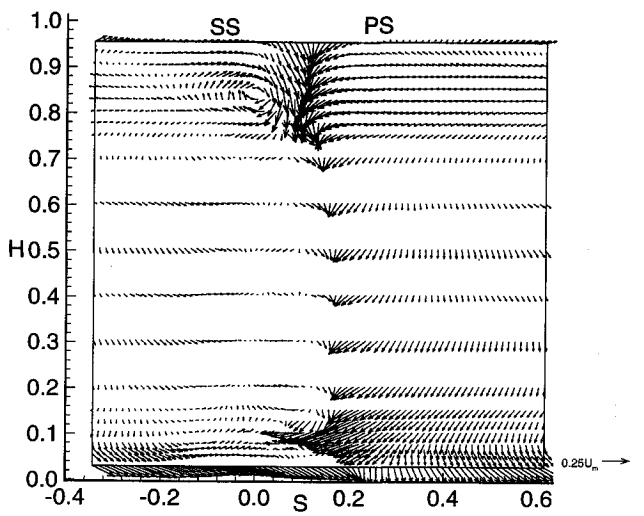

Fig. 11 Secondary velocity vectors at $X/C = 1.09$.

vortex can be seen clearly, near $H = 0.8$ at $X/C = 1.09$, although at $X/C = 1.025$ the radial inward flow is so strong that the vortical motion cannot be seen. It is also probable that the secondary flow has not yet rolled up into a discrete vortex at $X/C = 1.025$. Since the pressure side leg of the horseshoe vortex has the same direction of rotation as the passage vortex, this vortex could be a combination of the passage vortex and the pressure side leg of the horseshoe vortex. Other researchers such as Langston[8] and Sieverding[9] believe that the pressure side leg of the horseshoe vortex merges with the passage vortex, and the results here do not show otherwise. There is no evidence of the suction side leg of the horseshoe vortex near the casing (which would rotate opposite to the passage vortex). Very close to the passage vortex, there is a vortical motion in the counterclockwise direction on the pressure side of the wake (this will be called the counter-rotating vortex). This is formed by the interaction of the passage vortex with the wake.

The radial flow is directed inward over almost the whole inviscid flowfield. This is because of the radial inward lean of the nozzle trailing edge, discussed earlier, which causes this flow movement toward the hub. The overturning on the suction side and the underturning on the pressure side can be clearly seen at the wake center. The radial inward flow is stronger in the wake than in the freestream, which is due to an imbalance of the centrifugal force and the pressure gradient close to the surface of the blade. The tangential velocity decreases as the surface of the blade is approached, and thus the centrifugal force decreases, while the radial pressure gradient remains nearly constant. This imbalance between the centrifugal and the pressure forces set up a radial inward flow, which continues even in the wake. This radial inward flow is in the same direction as those induced by the casing passage vortex and, thus, it augments the casing passage vortex. At the hub there is also evidence of the passage vortex at $X/C = 1.025$. But the radial inward flow in the wake near the hub is in the opposite direction to those caused by the passage vortex, and thus the radial inward flow seems to counteract those induced by the hub passage vortex. At $X/C = 1.09$, the hub passage vortex seems to have dissipated, although the casing passage vortex remains strong. This is a result of the interaction of the hub passage vortex with the rotating hub that is located just downstream of this location. The hub rotation is toward increasing S in this figure.

Streamwise Vorticity

Even though the isocline angle plots and the secondary flow vector plots are useful in identifying vortices, they have their limitations. The isoclinal angle plots cannot determine the sign of the vortex, whereas the secondary flow vectors can change depending on what the primary flow is defined to be. A more logical approach in identifying both the vortices and their sign is to examine the strength of the streamwise vorticity. But this method has its problems, too. The scatter in experimental data can cause unrealistic gradients and, therefore, false levels of vorticity. But, usually the biggest problem is that the axial distance between the data points is much larger than the radial and tangential distances between the data points, thus, the streamwise vorticity cannot be found explicitly since it would involve gradients of velocity in the axial direction. But in this experiment the axial distance between the measurement planes is small (7 mm) and comparable to the tangential distance (1 mm) and average radial distance (5 mm) between the data points.

The components of vorticity in the axial, tangential, and radial directions are given by

$$\omega_x = \frac{1\partial V_r}{r\partial\Theta} - \frac{\partial(rV_\theta)}{r\partial r}, \quad \omega_\theta = \frac{\partial V_x}{\partial r} - \frac{\partial V_r}{\partial x}, \quad \omega_r = \frac{\partial V_\theta}{\partial x} - \frac{1\partial V_x}{r\partial\theta} \qquad (2)$$

Knowledge of V_r, V_θ, and V_x enables the calculation of the vorticity components. The streamwise vorticity can then be derived from the equation

$$\omega_s = \omega_x \cos \beta_p + \omega_\theta \sin \beta_p + \omega_r \sin \alpha \qquad (3)$$

The primary flow angle is set equal to the design exit flow angle (70.0 deg).

The contour plots of streamwise vorticity $\omega_s C/V_{x1}$ at $X/C = 1.025$ and $X/C = 1.09$ are given in Figs. 12 and 13, respectively. The existence of a strong casing passage vortex is clearly seen in these figures. The large positive vorticity (peak magnitude of 17 at $X/C = 1.025$ and 18 at $X/C = 1.09$) near the casing corresponds to the passage vortex. At the hub, the passage vortex is indicated by the large negative vorticity. The magnitude of peak vorticity at the center of the vortex at $X/C = 1.025$ (-15) is similar in magnitude to the peak vorticity at the casing, which demonstrates that the hub passage vortex is similar in strength to the casing passage vortex at $X/C = 1.025$. The magnitude of peak negative vorticity at the hub decreases by 33% from $X/C = 1.025$ to $X/C = 1.09$, which agrees with the secondary flow vectors that the hub passage vortex is decreasing in strength as it moves downstream of the nozzle trailing edge.

At $X/C = 1.025$, there are two negative vorticity regions near the casing. The larger (in area) of the two (peak magnitude of -7) is due to the counter-rotating vortex (which is caused by the interaction of the passage vortex and the wake). The smaller negative vorticity region (peak magnitude of -11) located just below the casing passage vortex, possibly could be the suction side leg of the horseshoe vortex. At $X/C = 1.09$ there is only one negative vorticity region near the casing. This vortex is also due to the interaction of the passage vortex with the wake. The small negative vorticity region seen at $X/C = 1.025$ seems to have disappeared at $X/C = 1.09$. It is possible that this vortex has either merged with the large negative vorticity region between the two axial planes or has been dissipated by its contact with the casing passage vortex.

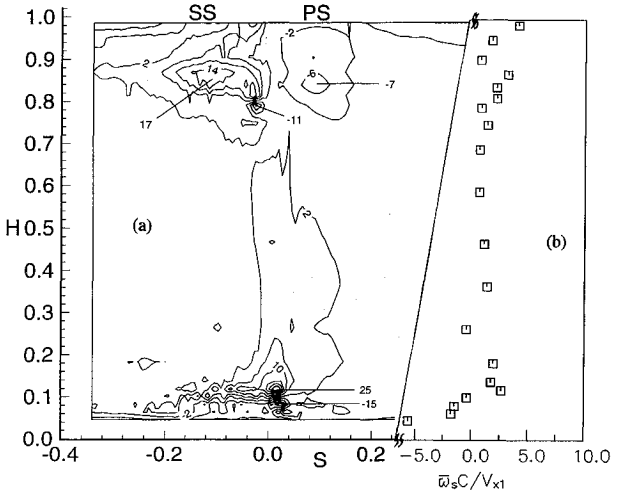

Fig. 12 Secondary vorticity at $X/C = 1.025$: a) local secondary vorticity $\omega_s V_{x1}/c$ contours and b) pitchwise-average $\bar{\omega}_s V_{x1}/c$ distribution.

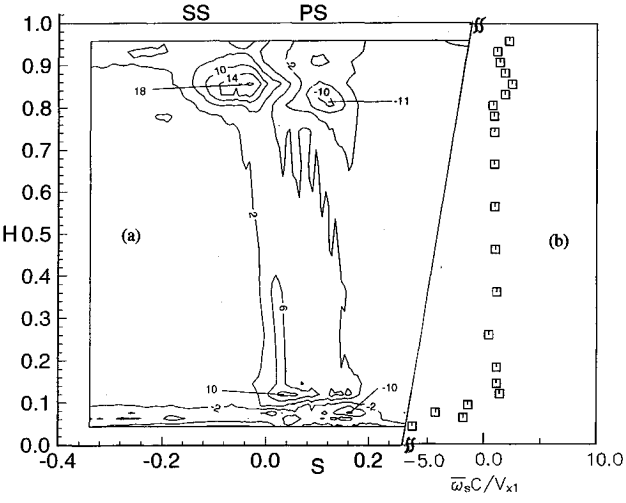

Fig. 13 Streamwise vorticity at $X/C = 1.09$: a) local secondary vorticity $\omega_s V_{x1}/c$ contours and b) pitchwise-average $\bar{\omega}_s V_{x1}/c$ distribution.

The pitch-averaged vorticity $\bar{\omega}_s C/V_{x1}$ plots are also shown in Figs. 12 and 13 for $X/C = 1.025$ and 1.09, respectively. Outside of the secondary flow regions the pitch-averaged vorticity is positive due to the over- and underturning regions in the wake. A large positive vorticity region occurs at $H = 0.1$, which is a result of the vortex formed by the interaction of the passage vortex and the wake. Moving closer to the hub, the vorticity becomes negative due to the existence of the passage vortex. The maximum negative vorticity occurs next to the hub and is a result of the interaction of the flow with the rotating hub. The variation in vorticity is not as large near the casing as it is near the hub, because the passage vortex and the counter-rotating vortex are side-by-side (at the same radial location) near the casing instead of at different radial locations as they are near the hub. The high positive vorticity at $H = 0.85$ is due to the passage vortex.

Near the wake center from $H = 0.7$ to $H = 0.1$, there is a positive vorticity region that corresponds to the over- and underturning regions in the wake. There is a positive vorticity peak at $H = 0.1$, which is caused by the interaction of the passage vortex and the wake. The peak magnitude of this positive vorticity decreases from 25 at $X/C = 1.025$ to 11 at $X/C = 1.09$. This is also a result of the interaction of the flow near the hub with the rotating hub.

Comparison of the peaks in streamwise vorticity with the total pressure loss contours (Fig. 3) shows that the peak total pressure loss does not occur at the peak vorticity location, but occurs somewhere between the positive and negative vorticity peaks. This is contrary to the results of linear cascades where the loss peaks coincide with the vorticity peaks (vortex centers).[19,20] The interaction between the secondary flow vortices and the wake causes the accumulation of the low momentum and energy endwall boundary-layer fluid into these two locations.

Six criteria are used to determine the existence of a vortex in the flowfield. These are high total pressure loss, low static pressure, high vorticity, over- and underturning of yaw angle, positive and negative radial flow angles, and vortical motion in the secondary flow vectors. A vortex exists when these six things occur at the same position in the flowfield. The existence of the passage vortices at both the hub and the casing are confirmed since they meet all six criteria. On the other hand, the existence of the suction side leg of the horseshoe vortex is more doubtful. There is no evidence for its existence at the hub. While at the casing there is a region of high negative vorticity at $X/C = 1.025$ that could correspond to the suction side leg of the horseshoe vortex, the other criteria are not met. Thus, its existence cannot be proven conclusively.

Nozzle Wake Characteristics

The static pressure variation across the wake for different radii at $X/C = 1.025$ is shown plotted in Fig. 14. Starting from the pressure side, the static pressure coefficient decreases sharply until the wake center, after which it increases rapidly across the suction side of the wake. A decrease in ψ_p indicates an increase in static pressure, because this is an accelerating flow. A hump at the suction side wake edge (A) has been caused by the overturning on the suction side, while the dip in static pressure coefficient on the pressure side wake

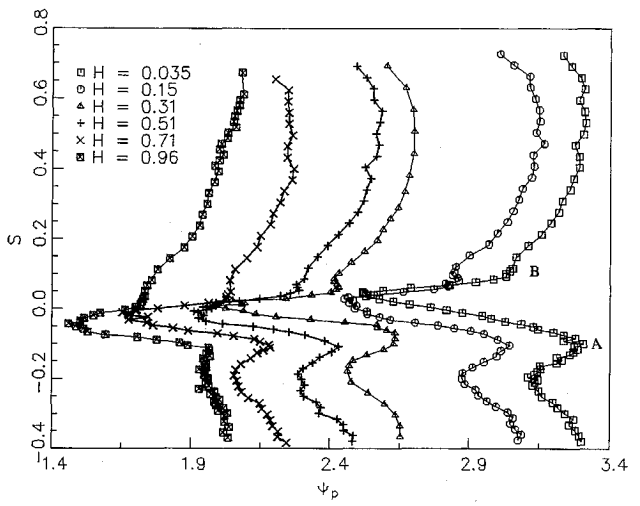

Fig. 14 Static pressure variation at $X/C = 1.025$.

edge (B) is caused by the underturning on the pressure side of the wake.

The strong radial pressure gradient is evident with the static pressure decreasing more than 35% as one goes from the tip to the hub. The static pressure variation across the wake is as high as 20–25% of the value in the freestream. This is consistent with the measurements of Lakshminarayana and Davino[21] who found similar static pressure gradients across the wake of a compressor inlet guide vane.

The existence of pressure gradients across the wake has been explained for a compressor rotor blade by Ravindranath and Lakshminarayana,[3] and can be comprehended by examining the equation of motion in a streamwise s and normal n coordinate system. The equation can be approximately written as

$$\frac{1}{\rho}\frac{\partial p}{\partial n} \approx \frac{V_s^2}{R_c} + \frac{\partial}{\partial n}(\overline{\nu_n'^2}) + \frac{\partial}{\partial s}(\overline{\nu_n'\nu_s'}) \qquad (4)$$

where n is the direction normal to the streamline, V_s is the streamwise velocity, R_c is the radius of curvature of the streamline, and (ν_n') is the turbulent fluctuation in the n direction, and $\overline{\nu_n'\nu_s'}$ is the turbulent shear stress. It is clear from the above equation that in addition to the centrifugal force, the gradient of turbulent intensity in the n direction has a major influence on the pressure gradient $\partial p/\partial n$. The static pressure gradient is caused by the flow curvature, velocity change, turbulence intensity, and possibly separated flow in the trailing-edge region.

Figures 15a and 15b show the total velocity profiles for $X/C = 1.025$. The plot indicates that the suction surface boundary layer is thicker than the pressure surface boundary layer. This is consistent with the boundary-layer data in a Turbine cascade presented by Bammert and Sandstede.[22] Several interesting observations can be made. The wake at $H = 0.98$ is well-behaved. The influence of interaction between the wake and the secondary flow can be seen in the wake data at $H = 0.870$ to $H = 0.810$. The two distinct troughs from $H = 0.870$ and 0.840 indicate that the wake and secondary flows are still distinct, and they are likely to merge as the flow progresses downstream. The region near $H = 0.810$ is the location of the strongest secondary flow/vorticity, and here, there is clear evidence of interaction between the wake and vortex resulting in a thick shear layer on the suction side. The region from $H = 0.766$ to 0.150 has a well-behaved wake and the secondary flow/vortex interaction with the wake is again evident below this region. In general, the wake defect is higher in the secondary flow regions.

A knowledge of the rate of decay for the wake defect is necessary for an understanding of the rotor-stator interaction.

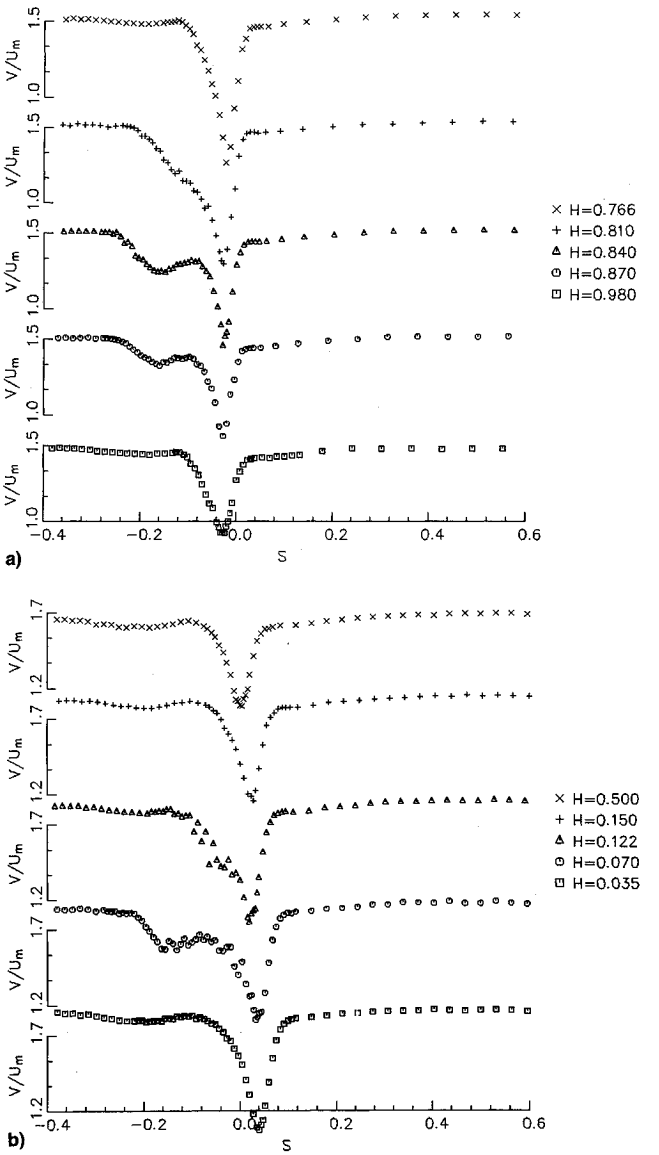

Fig. 15 Total velocity profiles of $X/C = 1.025$.

The decay of the velocity defect is influenced by the pressure gradient, turbulence intensity, curvature, and viscous effects. The endwall secondary flow and passage vortices also have an effect on the wake decay. The velocity defect plotted in Fig. 16 is based on the maximum and minimum velocity in the wake, plotted against $Z/\cos\beta_o$, where β_o is the local value of the vane outlet angle. This corresponds approximately to the streamwise distance downstream of the nozzle.

The authors' data at midspan is compared with data from other sources. Goldman and Seasholtz[6,23] did their measurements in an annular cascade, whereas Dring et al.[7] measured the wake behind the nozzle with a rotor-stator spacing of 50% of nozzle axial chord. Sitaram and Govardhan[5] did their measurements in a linear turbine rotor cascade. Ho and Lakshminarayana[24] computed the flowfield in a linear turbine rotor cascade. Raj and Lakshminarayana[2] measured the wake behind a linear cascade of compressor blades and developed a correlation. They found that the wake from a compressor cascade decays slower than that of a flat plate, cylinder, or a symmetrical airfoil. They attributed this to the fact that the wake edge velocity decelerates in a compressor cascade, thus causing an adverse pressure gradient, which causes the wake to decay slower. The wake decays rapidly close to the trailing edge and less rapidly farther downstream. Lakshminarayana and Davino[21] state that the rapid decay rate close to the trailing edge is due to pressure gradients, high-turbulence in-

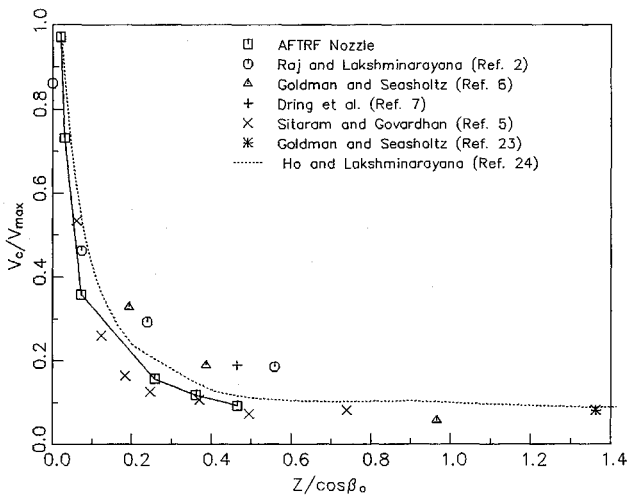

Fig. 16 Decay of total velocity defect with streamwise distance (midspan).

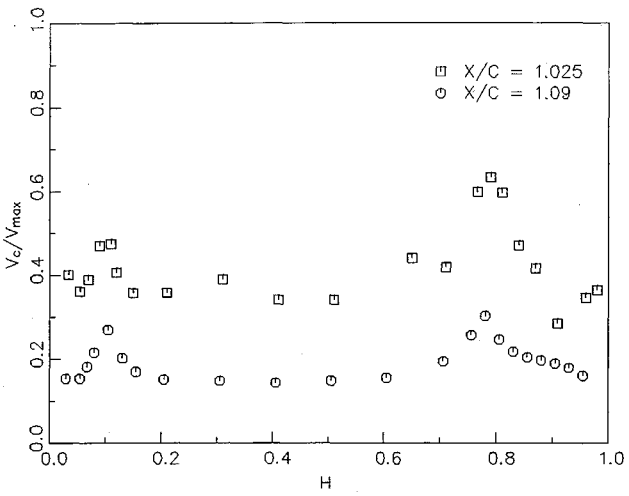

Fig. 17 Radial variation of total velocity defect in the wake.

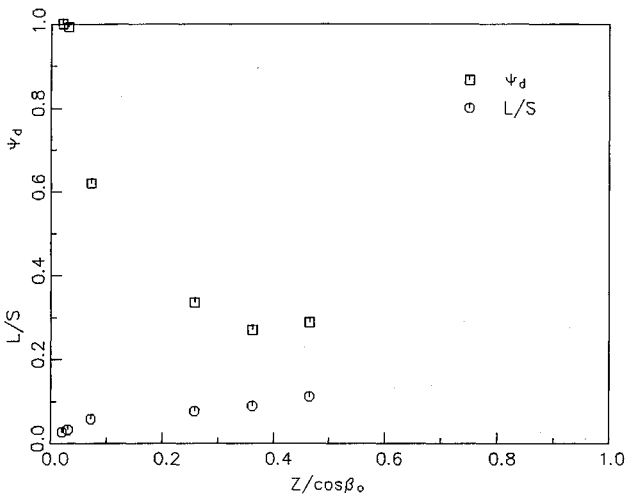

Fig. 18 Variation of static pressure and semiwake width with streamwise distance.

tensities, and wake centerline curvature. The wake data from Dring's cascade and Goldman's cascade decay slightly faster than Raj's cascade. This is because the wake edge velocity decay is almost zero for the turbine nozzle and rotor cascades (not shown), hence, the streamwise pressure gradient in the edge of the wake is zero. And according to Hill,[25] wakes in an adverse pressure gradient will decay slower than wakes in the presence of zero pressure gradient. In addition, the wake in the presence of favorable pressure gradient is found to decay faster. Also, the increased loading on the nozzle vanes compared to Raj and Lakshminarayana's compressor cascade could cause an increase in the wake decay rate.

The data from the AFTRF nozzle, on the other hand, have a much more rapid decay rate than the compressor cascade wake or Goldman and Seasholtz's turbine nozzle cascade. This is due to the presence of the rotor downstream at a very small rotor-stator axial spacing (rotor-stator spacing is 20% of the nozzle axial chord). The relative motion between the rotor and the stator causes periodic variations in the potential flowfield around the blades. This unsteadiness causes the wake to decay faster than the wake of a cascade with no rotor behind it. The nozzle wake is also affected by the favorable pressure gradient in the rotor, which causes it to decay faster. Even though the nozzle of Dring et al.[7] has a rotor downstream, the rotor-stator spacing is much larger (50% nozzle axial chord) than that of the AFTRF nozzle. Thus, the potential flow interaction will have less effect on the nozzle wake in Dring et al.'s[7] case. Ho and Lakshminarayana's turbine rotor cascade (computed) also decays faster than the compressor wake or Dring's or Goldman's nozzles. This is due to the fact that the loading on the rotor was much higher than on the nozzles, since the rotor turning is 110 deg, although the turning is around 70 deg for all the nozzle data shown in Fig. 16. Sitaram and Govardhan's turbine rotor wake decays a little faster than Ho and Lakshminarayana's rotor cascade since their loading is higher (rotor turning is 120 deg for Sitaram and Govardhan's cascade).

The decay of maximum (absolute) radial velocity (not shown) is constant from the trailing edge until $Z/\cos\beta = 0.30$, and then decreases slightly. The magnitude is similar to the radial velocity decay of a compressor stator reported by Lakshminarayana and Davino.[21] Figure 17 shows the radial variation of total velocity defect at the centerline at $X/C = 1.025$ and $X/C = 1.09$. Caution should be used in interpreting this data. Since the wake belongs to different blade sections with varying in boundary-layer growth, the variation of defect in the radial direction should not be interpreted as the decay rate. The variation of wake defect with spanwise distance is clearly seen from this plot. There are two regions where the wake defect is larger than the others, one centered around $H = 0.1$, and the other centered around $H = 0.8$. This is the region where the secondary flow vortices are located, and the interaction of these with the wake results in deeper and wider wakes. Thus, the wake defect will be larger at these locations. The rate of wake decay between $X/C = 1.025$–1.09 is almost constant from the hub to $H = 0.6$, and then increases until the maximum decay rate is reached at $H = 0.8$. This is due to effect of the two counter-rotating vortices at this location.

The variation of the semiwake width at midspan with streamwise distance is shown in Fig. 18. The semiwake width is defined as the width of the wake at half the defect of total velocity. The semiwake width grows rapidly close to the trailing edge and more gradually farther downstream. This growth is due to the exchange of momentum, mass, and energy on both sides of the wake. The variation of the maximum static pressure difference ψ_d across the wake at midspan is shown vs streamwise distance in Fig. 18. The value of ψ_d decays to 50% its value within a streamwise distance of 10% chord. This rapid decay is caused by the intense mixing and high-turbulence intensities that occur close to the trailing edge.[3] The decay rate levels off as the wake moves downstream of the trailing edge, reaching a value of 28% of its value at the trailing edge within a streamwise distance of 40% of chord. Most researchers assume that the static pressure is uniform at the trailing edge, both inside the wake and in the free-stream. This assumption is not valid in view of the data shown in Figs. 18 and 14.

Concluding Remarks

A complete flowfield survey was carried out at two axial locations of $X/C = 1.025$ and $X/C = 1.09$ downstream of the nozzle in an axial flow turbine facility. The results showed a strong radial inward flow, which was more pronounced in the wake. Secondary flow vortices have been identified near the casing and the hub. These vortices are on the suction side of the wake and are made up of either the passage vortex or a combination of the passage vortex and the pressure side leg of the horseshoe vortex. There is also indication of other vortices located in the wake center, near the casing and the hub. They rotate opposite to the passage vortices and are caused by the interaction of the passage vortices and the wake. On the other hand, there is conflicting evidence on the existence of the suction side leg of the horseshoe vortex. While there is no evidence for its existence at the hub, there is a region of negative vorticity near the casing at $X/C = 1.025$ that could correspond to this vortex, but the secondary flow vectors do not show the existence of a vortex. More work needs to be done to determine the existence of the suction side leg of the horseshoe vortex.

A circumferential survey was also done at three other locations at midspan to determine the wake decay characteristics. The AFTRF nozzle wake decays much faster than a compressor cascade wake, an annular turbine nozzle cascade wake, or a turbine nozzle wake with a large rotor-stator spacing. This is due to the presence of a rotor in close vicinity, as well as the influence of a favorable pressure gradient downstream.

Acknowledgments

This work was supported by NASA Lewis Research Center, Cleveland, Ohio, through Grant NSG3-555, with R. Boyle, K. Civinskas and J. Schwab as technical monitors.

References

[1]Dring, R. P., Joslyn, H. D., Hardin, L. W., and Wagner, J. H., "Turbine Rotor-Stator Interaction," *Journal of Engineering for Power*, Vol. 104, Oct. 1982, pp. 729–742.

[2]Raj, R., and Lakshminarayana, B., "Characteristics of the Wake Behind a Cascade of Airfoils," *Journal of Fluid Mechanics*, Vol. 61, Pt. 4, 1973, pp. 707–730.

[3]Ravindranath, A., and Lakshminarayana, B., "Mean Velocity and Decay Characteristics of the Near and Far-Wake of a Compressor Rotor Blade of Moderate Loading," *Journal of Engineering for Power*, Vol. 102, July 1980, pp. 535–548.

[4]Mee, D. J., Baines, N. C., Oldfield, M. L. G., and Dickens, T. E., "An Examination of the Contribution to Loss on a Transonic Turbine Blade in Cascade," *Journal of Turbomachinery*, Vol. 114, Jan. 1992, p. 155.

[5]Sitaram, N., and Govardhan, M., "Effect of Incidence Angle on Wake Characteristics of High Deflection Turbine Rotor Linear Cascade," 9th Australasian Fluid Mechanics Conference, Auckland, New Zealand, Dec. 1986.

[6]Goldman, L. J., and Seasholtz, R. G., "Laser Anemometer Measurements and Computations in an Annular Cascade of High Turning Core Turbine Vanes," NASA TP 3252, July 1992.

[7]Dring, R. P., Joslyn, H. D., and Blair, M. F., "The Effects of Inlet Turbulence and Rotor/Stator Interactions on the Aerodynamics and Heat Transfer of a Large-Scale Rotating Turbine Model," Vol. 4, NASA-CR-179469, Nov. 1987.

[8]Langston, L. S., "Crossflows in a Turbine Cascade Passage," *Journal of Engineering for Power*, Vol. 102, No. 4, 1980, pp. 866–874.

[9]Sieverding, C. H., "Recent Progress in the Understanding of Basic Aspects of Secondary Flows in Turbine Blade Passages," *Journal of Engineering for Gas Turbines and Power*, Vol. 107, April 1985, pp. 248–257.

[10]Sharma, O. P., and Butler, T. L., "Predictions of Endwall Losses and Secondary Flows in Axial Flow Turbine Cascades," *Journal of Turbomachinery*, Vol. 109, April 1987, pp. 229–236.

[11]Lakshminarayana, B., Camci, C., Halliwell, I., and Zaccaria, M., "Investigation of Three Dimensional Flow Field in a Turbine Including Rotor/Stator Interaction, Part 1: Design, Development and Performance of Turbine Facility," AIAA Paper 92-3325, July 1992.

[12]Zaccaria, M., and Lakshminarayana, B., "Investigation of Three Dimensional Flow Field in a Turbine Including Rotor/Stator Interaction, Part 2: Three Dimensional Flow Field at the Exit of the Nozzle," AIAA Paper 92-3326, July 1992.

[13]Yamamoto, A., and Yanagi, R., "Production and Development of Secondary Flows and Losses Within a Three Dimensional Turbine Stator Cascade," *International Journal of Turbo and Jet Engines*, Vol. 3, No. 1, 1986, pp. 79–90.

[14]Hunter, I. H., "Endwall Boundary Layer Flows and Losses in an Axial Turbine Stage," *Journal of Engineering for Power*, Vol. 104, Jan. 1982, pp. 184–193.

[15]Kacker, S. C., and Okapuu, U., "A Mean Line Prediction Method for Axial Flow Turbine Efficiency," *Journal of Engineering for Power*, Vol. 104, Jan. 1982, pp. 111–119.

[16]Dunham, J., "A Review of Cascade Data on Secondary Losses in Turbines," *Journal of Mechanical Engineering Sciences*, Vol. 12, No. 1, 1970, pp. 48–59.

[17]Moore, J., and Adhye, R., "Secondary Flows and Losses Downstream of a Turbine Cascade," *Journal of Engineering for Gas Turbines and Power*, Vol. 109, 1985, pp. 961–969.

[18]Binder, A., and Romey, R., "Secondary Flow Effects and Mixing of the Wake Behind a Turbine Stator," American Society of Mechanical Engineers, ASME Paper 82-GT-46, April 1982.

[19]Gregory-Smith, D. G., Graves, C. P., and Walsh, J. A., "Growth of Secondary Losses and Vorticity in an Axial Turbine Cascade," *Journal of Turbomachinery*, Vol. 110, Jan. 1988, pp. 1–8.

[20]Hodson, H. P., and Dominy, R. G., "Three-Dimensional Flow in a Low-Pressure Turbine Cascade at Its Design Condition," *Journal of Turbomachinery*, Vol. 109, April 1987, pp. 177–185.

[21]Lakshminarayana, B., and Davino, R., "Mean Velocity and Decay Characteristics of the Guidevane and Stator Blade Wake of an Axial Flow Compressor," *Journal of Engineering for Power*, Vol. 102, Jan. 1980, pp. 50–60.

[22]Bammert, K., and Sandstede, H., "Measurements of the Boundary Layer Development Along a Turbine Blade with Rough Surfaces," American Society of Mechanical Engineers Paper 80-GT-40, 1980.

[23]Goldman, L. J., and Seasholtz, R. G., "Laser Anemometer Measurements in an Annular Cascade of Core Turbine Vanes and Comparison with Theory," NASA TP 2018, June 1982.

[24]Ho, Y. H., and Lakshminarayana, B., "Computational Modelling of Three-Dimensional Flow Through a Turbine Rotor Cascade with Strong Secondary Flows," American Society of Mechanical Engineers Paper 94-GT-136, 1994.

[25]Hill, P. G., Schwab, U. W., and Senoo, Y., "Turbulent Wakes in Pressure Gradients," *Journal of Applied Mechanics*, Dec. 1963, pp. 518–524.